Numerical modelling of an optical belt sorter using a DEM–CFD approach coupled with particle tracking and comparison with experiments

C. Pieper [a,*], F. Pfaff [b], G. Maier [c], H. Kruggel-Emden [d], S. Wirtz [a], B. Noack [b], R. Gruna [c], V. Scherer [a], U.D. Hanebeck [b], T. Längle [c], J. Beyerer [c]

[a] Ruhr-University of Bochum, Universitaetsstrasse 150, 44780 Bochum, Germany
[b] Karlsruhe Institute of Technology, Adenauerring 2, 76131 Karlsruhe, Germany
[c] Fraunhofer Institute of Optronics, System Technologies and Image Exploitation, Fraunhoferstrasse 1, 76131 Karlsruhe, Germany
[d] Technical University of Berlin, Ernst-Reuter-Platz 1, 10523 Berlin, Germany

A B S T R A C T

State-of-the-art optical sorting systems suffer from delays between the particle detection and separation stage, during which the material movement is not accounted for. Commonly line scan cameras, using simple assumptions to predict the future particle movement, are employed. In this study, a novel prediction approach is presented, where an area scan camera records the particle movement over multiple time steps and a tracking algorithm is used to reconstruct the corresponding paths to determine the time and position at which the material reaches the separation stage. In order to assess the benefit of such a model at different operating parameters, an automated optical belt sorter is numerically modelled and coupled with the tracking procedure. The Discrete Element Method (DEM) is used to describe the particle–particle as well as particle–wall interactions, while the air nozzles required for deflecting undesired material fractions are described with Computational Fluid Dynamics (CFD). The accuracy of the employed numerical approach is ensured by comparing the separation results of a predefined sorting task with experimental investigations. The quality of the aforementioned prediction models is compared when utilizing different belt lengths, nozzle activation durations, particle types, sampling frequencies and detection windows. Results show that the numerical model of the optical belt sorter is able to accurately describe the sorting system and is suitable for detailed investigation of various operational parameters. The proposed tracking prediction model was found to be superior to the common line scan camera method in all investigated scenarios. Its advantage is especially profound when difficult sorting conditions, e.g. short conveyor belt lengths or uncooperative moving bulk solids, apply.

1. Introduction

With continuously growing material streams, the handling and processing of bulk solids is becoming increasingly important. The efficient separation of materials can be achieved by various procedures, depending on the properties of the respective bulk solid. When utilizing optical sorting, optical features like color, texture or even shape and size are determined and used for particle separation [1–3]. Optical sorters are becoming increasingly important for the processing of mineral raw materials [4–7] as well as in the fields of food technology [1,8–10] and recycling [11–15]. In most industrial applications, the sorting aim is to separate low-quality materials from high-quality materials, resulting in an accept or reject task. Corresponding systems usually include components for transportation, a sensor for the detection of the particle properties and a data processing unit where this information is evaluated in real-time and subsequently used to control a separation mechanism [16].

Although optical sorting systems are commonly used in various fields of application, detailed scientific studies are fairly scarce. Most research is focused on the technical or economical assessment of optical sorters for specific sorting tasks like the separation during lithium processing [5], metal recycling [12], magnesite processing [4], sorting of quartz pebbles [2], ceramic materials [6] or other mineral resources [7], grain processing [3,8], the sorting of household waste [17], processing in the fishing industry [10,18], construction rubble recycling [19] and plastic recycling [15,20]. Other studies concentrate on individual sorter components, especially on the sensor technology employed for the optical detection [21–23], advise procedural modifications [13] or aim towards identifying new optical features [9]. A review paper was published, which mostly regards optical sorting as part of other sorting processes and also gives concrete examples where they can be utilized to their full advantage [11].

* Corresponding author.
E-mail address: pieper@leat.rub.de (C. Pieper).

Research focusing on the connection between system parameters, throughput and resulting sorting quality is equally rare and the few existing studies investigate the correlation between the occupancy rate, throughput, size of individual particles and the sorting quality [24,25]. There is also hardly any focus on detailed processes within the sorter, like the ejection of particles with jets of compressed air [26]. Furthermore, the potential of available simulation procedures like the Discrete Element Method (DEM) coupled with Computational Fluid Dynamics (CFD), which allows the modelling of particle–particle, particle–wall as well as particle–fluid interactions within the system, is hardly utilized [27]. The DEM–CFD has already been successfully employed to model other material separators like screens [28–31] and cyclones [32–34].

In this study, an automated optical belt sorter is investigated, see Fig.1 a. State-of-the-art optical belt sorters used in industrial applications commonly employ line scan cameras to localize and classify individual particles in the material stream. The particle type predetermined for separation is then deflected with bursts of compressed air emitted by nozzles aligned orthogonally to the transport direction of the conveyor belt. As can be seen inFig.1, a delay exists between the perception and separation of the material, which is required for the data processing. Consequently, there is no information on particle movement between these two stages. The prediction of when and where the particles reach the nozzle bar of the sorter is currently based on the assumption that all particles move in belt direction with an identical velocity. This simplification is sufficient for many bulk solids, however, materials that feature a more complex motion behavior and do not easily adapt to the speed and movement direction of the belt, pose a significant challenge. While the orthogonal movement of the so-called uncooperative bulk solids can be reduced by modifying the sorting system, e.g. employing longer conveyor belts or reducing material throughput, these changes often result in additional costs or induce other undesirable implications.

In order to improve the prediction of the material's movement after the detection stage and to avoid large scale sorter modifications, we propose the use of an area scan camera with appropriate algorithms [35,36]. The line scan camera is replaced with an area scan camera, which is positioned at the end of the conveyor belt, as shown in Fig.1 b. This setup enables the observation of individual particles over multiple time steps

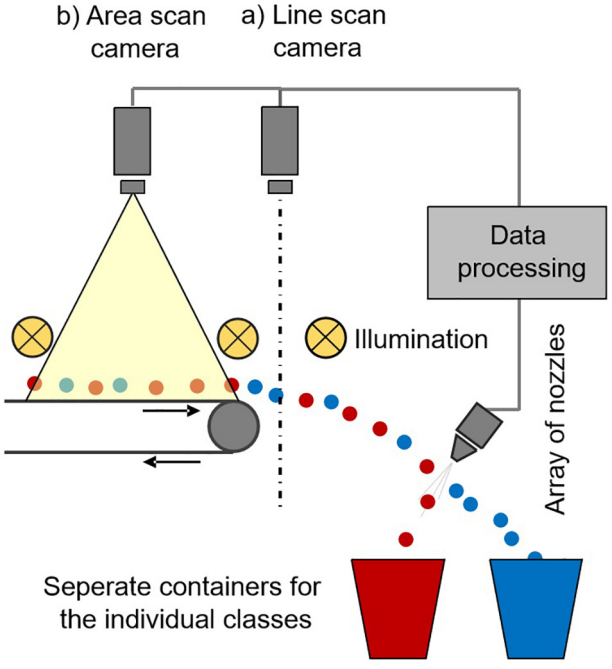

Fig.1. Illustration of on optical belt sorter, which can be equipped with a conventional line scan camera a)or an area scan camera b).

and the obtained information on material movement can be used for a more accurate prediction of the time and place the particles pass the separation stage. This concept is referred to as predictive tracking within this study. We have already validated the theoretical concept and functionality of the described approach using pre-recorded real image data [37] and presented concepts to maintain real-time capability [38]. In previous research, we have also shown that the DEM is able to accurately describe the impact of different operating parameters on particle movement within the optical sorter and presented the theoretical advantages of employing an area scan camera in conjunction with particle tracking [39].

In this study, the DEM is coupled with CFD to describe an entire optical sorter, including the particle–fluid interaction within the separation stage of the system. The model of the sorter is based on an existing modular sorting system, that consists of all of the features of an industrial-sized sorter, with the advantage of being easy to modify and operate. The geometry of the system's nozzle bar is meshed with ANSYS ICEM and CFD simulations of individual nozzles are performed. To ensure correct calculation, the fluid field velocity is compared with conducted experiments. Non-spherical particles, namely peppercorns, maize grains and coffee beans, are modelled with a multi-sphere method. Spheres of different sizes are merged to form a cluster to approximate complex particle shapes [40]. In order to ensure a good representation of the material and to determine the optimal particle interaction parameters required for the DEM simulations, e.g. Coulomb/rolling friction and the coefficient of normal restitution, static and dynamic simulations of particle collectives are performed and compared with corresponding experiments [41]. The overall quality of the sorter model is tested by defining a specific sorting task and comparing the sorting results obtained from the simulation with those of similar experiments.

The main aim of this study is not only to accurately model an optical sorting system, but also to test the presented tracking approach. For this reason, the tracking algorithm, which is realized as a MATLAB script, is coupled to the DEM–CFD simulation. The positions of all particles located in a predefined area on the conveyor belt, which resembles the space assessed by the area scan camera, are transferred from the DEM–CFD simulation to the tracking script at a predefined rate, which resembles the frame rate of the area scan camera in the experiment. The tracking script subsequently calculates the future motion of the particles after leaving the detection area, and information on the number of nozzles activated at specific times is transferred back to the simulation. By defining a sorting task and evaluating the subsequent sorting results, the employed tracking procedure is compared to utilizing a conventional line scan camera approach and an ideal constant velocity prediction, where the velocity of the particles at the end of the detection zone is directly taken from the DEM–CFD simulations. With this approach, the benefits of employing an area scan camera with particle tracking are investigated under different operating conditions. On the DEM–CFD side, the conveyor belt length, particle type and activation duration of the air nozzles are altered. The impact of utilizing different detection area dimensions and data sampling frequencies is investigated on the tracking side.

2. Numerical method

2.1. DEM–CFD approach

The Discrete Element Method (DEM) is used to model the particle–particle and particle–wall interactions within the optical sorting system. All calculations are performed with an in-houseDEM-code. Newton's and Euler's equations of motion are used to calculate the translational and rotational motion of every particle given by

$$m_i \frac{d^2 \vec{x}_i}{dt^2} = \vec{F}_i^{\,c} + \vec{F}_i^{\,g} + \vec{F}_i^{\,pf} \tag{1}$$

$$\hat{I}_i \frac{d\overrightarrow{W}_i}{dt} + \overrightarrow{W}_i \times \left(\hat{I}_i \overrightarrow{W}_i\right) = \Lambda_i^{-1} \overrightarrow{M}_i \tag{2}$$

with particle mass m_i, particle acceleration $d^2\overrightarrow{x}_i/dt^2$, contact force $\overrightarrow{F}_i^c$, gravitational force $\overrightarrow{F}_i^g$ and particle–fluid force $\overrightarrow{F}_i^{pf}$. The second equation gives the angular acceleration $d\overrightarrow{W}_i/dt$, angular velocity $\overrightarrow{W}_i$, external moment $\overrightarrow{M}_i$ resulting out of contact or particle–fluid forces, the inertia tensor $\hat{I}_i$ along the principal axis and the rotation matrix converting a vector from the inertial into the body fixed frame Λ_i^{-1}.

The non-spherical particles utilized in this study are modelled with a multi-sphere approach, where spheres of different sizes are merged to form a particle cluster to approximate the investigated complex particle shapes. The contact force laws are equal to those used for spherical particles [42] and are separated into a normal and tangential component. Alinear spring damper model is employed to obtain the normal component of the contact force

$$\overrightarrow{F}^n = k^n \delta \overrightarrow{n} + \gamma^n \overrightarrow{v}_{rel}^n, \tag{3}$$

where k^n is the spring stiffness, δ the virtual overlap, $\overrightarrow{n}$ a normal vector, γ^n a damping coefficientand $\overrightarrow{v}_{rel}^n$ the normal velocity in the contact point. The coefficient of normal restitution between particles e_{pp}^n, particles and walls e_{pw}^n and the employed time step determine the spring stiffnessk^n and the damping coefficient γ^n. The tangential forces are calculated by using a linear spring limited by the Coulomb condition

$$\overrightarrow{F}^t = \min\left(k^t \left|\overrightarrow{\xi}^t\right|, \mu_C \left|\overrightarrow{F}^n\right|\right) \overrightarrow{t} \tag{4}$$

Here k^t is the stiffness of a linear spring, μ_C is the friction coefficient, $\overrightarrow{\xi}^t$ is the relative tangential displacement and $\overrightarrow{t}$ is the tangential unit vector.

A rolling friction model devised by Zhou etal. [43], which considers the moments resulting from the rolling friction between particles as well as particles and walls, is included in the external moment resulting out of contact forces $\overrightarrow{M}_i$ described in Eq.(2)

$$\overrightarrow{M}_i^r = -\mu_r \left|\overrightarrow{F}^n\right| \frac{\overrightarrow{W}_i}{\left|\overrightarrow{W}_i\right|} \tag{5}$$

where μ_r is the coefficient of rolling friction, $\overrightarrow{F}^n$ the normal component of the contact force and $\overrightarrow{W}_i$ the angular velocity.

The compressed air nozzles used for the separation of the material stream are modelled with Computational Fluid Dynamics (CFD), where the Navier–Stokes equations are solved based on Finite Volume Method (FVM). For this purpose, both the fluid field and the enclosed nozzle are approximated with a detailed and locally refined hexagonal cell mesh. The equation of continuity and the equation of momentum are solved

$$\frac{\partial \rho_f}{\partial t} + \nabla\left(\rho_f \overrightarrow{u}_f\right) = 0 \tag{6}$$

$$\frac{\partial\left(\rho_f \overrightarrow{u}_f\right)}{\partial t} + \nabla\left(\rho_f \overrightarrow{u}_f \overrightarrow{u}_f\right) = -\nabla p + \nabla(\tau) + \rho_f \overrightarrow{g} \tag{7}$$

where $\overrightarrow{u}_f$ is the fluid velocity, ρ_f the fluid density, p the pressure and τ the fluid viscous stress tensor. The stress tensor τ can be written as

$$\tau = \mu_e \left[\left(\nabla \overrightarrow{u}_f\right) + \left(\nabla \overrightarrow{u}_f\right)^{-1}\right] \tag{8}$$

Here, μ_e is the effective viscosity determined from a k-ε model, which is commonly used to describe turbulent gas flows from nozzles [44–46].

In order to save computational time and due to the short activation durations of the nozzles, a one-way coupling is performed between the DEM and CFD to model the particle-fluid interaction in the sorting system. This means that the fluid field impacts the particle motion, but not vice versa. The fluid velocity is averaged in every CFD cell and the resulting fluid velocity field is transferred to the DEM upon initialization of the simulation. The influence of the fluid on the particles is considered in the DEM by the particle–fluid force described in Eq.(1), which equals the sum of all individual particle–fluid forces. A popular model devised by Di Felice [47] is employed, which is also suitable for complex shaped particles and is written as

$$\overrightarrow{F}_i^{pf} = \overrightarrow{F}_i^d + \overrightarrow{F}_i^{\nabla p} = \frac{1}{2}\rho_f \left|\overrightarrow{u}_f - \overrightarrow{u}_p\right| C_D A_\perp \varepsilon_f^{1-\chi}\left(\overrightarrow{u}_f - \overrightarrow{u}_p\right) \tag{9}$$

where $\overrightarrow{F}_i^d$ is the drag force, $\overrightarrow{F}_i^{\nabla p}$ the pressure gradient force, $\overrightarrow{u}_p$ the particle velocity, C_D the drag coefficient, $A_\perp$the cross-sectional area perpendicular to the flow, ε_f the local fluid porosity (representing the cell volume displaced by the particle) and χ a correction factor. χ is a function of the particle Reynolds-number

$$Re = \varepsilon_f \rho_f d_p \left|\overrightarrow{u}_f - \overrightarrow{u}_p\right| / \mu_f \tag{10}$$

and is calculated as

$$\chi = 3.7 - 0.65 \exp\left(-\frac{(1.5 - \log(Re))^2}{2}\right) \tag{11}$$

Here, d_p is the particle diameter and μ_f the fluid viscosity. The drag coefficient is derived from a correlation proposed by Hölzer and Sommerfeld [48] and is written as

$$C_D = \frac{8}{Re}\frac{1}{\sqrt{\phi_\perp}} + \frac{16}{Re}\frac{1}{\sqrt{\phi}} + \frac{3}{\sqrt{Re}}\frac{1}{\phi^{3/4}} + 0.42 \times 10^{0.4(-\log(\phi))^{0.2}}\frac{1}{\phi_\perp} \tag{12}$$

where $\phi_\perp$ is defined as the ratio between the cross-sectional area of a volume equivalent sphere and the projected cross-sectional area of the considered particle perpendicular to the flow. ϕ is the sphericity, namely the ratio between the surface area of a volume equivalent sphere and the surface area of the particle considered.

2.2. Tracking algorithm

By the use of an area scan camera, we can observe the particles, also denoted as targets, at multiple points in time and generate an individual prediction for each particle's future motion. In contrast to line scan camera systems, in which the prediction is based on the assumption that all particles move in belt direction and with equal velocities, this approach can deliver much more accurate information on when and where the material reaches the separation stage of the sorter.

In real-world applications, an image processing routine is first used to extract the centroids of the individual particles on which the tracking procedure is conducted. However, as we perform tracking on simulated data in this study, we can omit the image processing component and directly consider the challenge of tracking particles based on position data.

The tracking procedure allows the reconstruction of the trajectory of the particles based on position measurements at regular time intervals. The particles are only tracked on the two-dimensional plane of the conveyor belt. In order to predict the particle's future position and velocity, a constant velocity model [49] is employed. In order to track the particles in the observed system, a Kalman filter [50], which consists of two parts, is utilized. The first part is the prediction step, in which the

motion model is used to make a prediction of the particle position and velocity in the next time step. The second part, referred to as update step, is used to refine this prediction. In order to use such a filter, linear models for the measurements and the motion of the particles are required. These models are introduced in the following.

The state of a single target, in our case consisting of the position and velocity of the individual particle, can be described with the vector-valued state $\boldsymbol{x}_k$, which is given as

$$\boldsymbol{x}_{-k} = [\boldsymbol{x}_k, \dot{\boldsymbol{x}}_k, \boldsymbol{y}_k, \dot{\boldsymbol{y}}_k]^{\mathrm{T}} \tag{13}$$

Here $\boldsymbol{x}_k$ and$\boldsymbol{y}_k$ are the position components, $\dot{\boldsymbol{x}}_k$ and $\dot{\boldsymbol{y}}_k$ the velocity components, and T denotes the transpose sign. The state of the particle at the next time step is calculated as

$$\boldsymbol{x}_{-k+1} = \mathbf{A}_k \boldsymbol{x}_{-k} + \mathbf{B}_k \boldsymbol{w}_{-k} \tag{14}$$

where $\boldsymbol{w}_k$ describes the noise term, which is a stocastically modelled deviation between the actual system behavior and our model thereof, $\mathbf{A}_k$ describes how the system changes from one time step k to $k+1$ and $\mathbf{B}_k$ describes how the noise term effects the state. We assume our model to be time-invariant, i.e.,$\mathbf{A}_k = \mathbf{A}$ and $\mathbf{B}_k = \mathbf{B}$, which are, for our constant velocity model.

$$\mathrm{A} = \begin{bmatrix} 1 & \Delta t & 0 & 0 \\ 0 & 1 & 0 & 0 \\ 0 & 0 & 1 & \Delta t \\ 0 & 0 & 0 & 1 \end{bmatrix} \text{ and } \mathrm{B} = \begin{bmatrix} (\Delta t)^2/2 & 0 \\ \Delta t & 0 \\ 0 & (\Delta t)^2/2 \\ 0 & \Delta t \end{bmatrix} \tag{15}$$

Here, Δt describes the time between two consecutive time steps, e.g., k and $k+1$.

In order to improve the calculated predictions, the particle positions are refined using the next set of particle positions obtained from the DEM in the update step of the filter. When considering a real-world scenario, the measured particle positions suffer from uncertainties due to errors and small deviations within the image processing routine. Although this is not the case with the data received from the DEM, an uncertainty variable $\boldsymbol{v}_k$, which is based on data obtained from corresponding experiments, is used for the calculations. As a detailed description of the update step of the Kalman filter would exceed the scope of this study, we refer the reader to [50,51].

Since in real-world applications only information on the particle position is obtained with the help of an area scan camera and no information on particle association between the recorded frames exists, correspondingly only the particle positions calculated with the DEM simulations are considered and no particle IDs are exchanged. Hence, we face the challenge to track multiple targets without labels, which is addressed in the field of multitarget tracking (MTT). The method employed in this study can be interpreted as a global nearest neighbor approach [52,53]. The global nearest neighbor chooses one assignment of measurements to tracks in each time step that minimizes the sum of the uncertainty-aware (Mahalanobis) distances over all track–measurement pairs. Describing the problem to find the most probable assignment using distances has multiple advantages. First, its visual interpretation is more intuitive. Second, the problem of minimizing the sum of costs can be interpreted as a linear assignment problem. For these, fast solvers such as the LAPJV [54] or auction algorithms [55] exist. In previous work [38,56], we have considered ways to ensure the real-time performance of our approach for real-world scenarios.

2.3. Coupling of DEM–CFD with tracking

The coupling between the DEM–CFD simulation and the particle tracking calculation, performed with a MATLAB script, is achieved through the automated exchange of information with text files. The information exchanged between the two programs is shown in Fig.2.

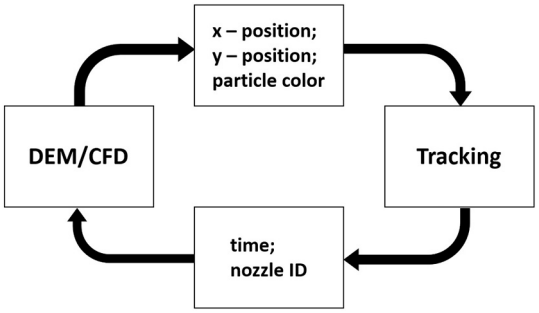

Fig.2. Connection between DEM–CFD and tracking procedure.

Before the simulation is started, an area is defined at the end of the conveyor belt which represents the zone seen by the area scan camera. During the simulation, the position and color of every particle in the defined area is written to a text file. This is done at a predefined sampling frequency, similar to that of the frame rate of the camera employed in real-world scenarios. Once the writing process is completed, the file is unlocked and the tracking program can access the information. Using sets of measurements at multiple time steps, tracks are generated, which are then used to predict the particles' future motion after leaving the detection area. It is important to note that, like in reality, there is no information exchanged that directly links a particle between two data sets, e.g. a particle ID. The association is purely performed within the tracking procedure.

When a particle exits the detection area, the calculated particle velocity and direction of movement is used to calculate the position and point in time in which the particle reaches the nozzle bar. The corresponding nozzle ID and time of activation are then written to a text file, which can then be accessed by the DEM–CFD simulation and used for the nozzle control.

3. Numerical and experimental setup

3.1. Optical belt sorter

The optical belt sorter investigated in this study is a modular version of a full sized industrial sorter, including all of the main hardware and software components. The experimental setup of the sorter is shown in Fig.3 a and can be equipped with an area or line scan camera. The system is run in batch operation and the bulk solids are initially placed in a particle container located on top of the vibrating feeder. Upon the start of the experiment or simulation, the container is lifted and the particles are channeled towards a slide by a vibrating feeder, which runs at a frequency of 50 Hz, at an angle of 25° and an amplitude of 0.315 mm, which can also be regulated. The bulk solids then reach the conveyor belt, which has an adjustable length of 0.3 m to 0.6 m and a width of 0.18 m. It runs at a constant velocity of 1.1 ms^{-1}. At the separation stage of the sorter, a nozzle bar consisting of 16 individual valves and operating at a gauge pressure of 1.2 bar, is installed. Here, the particles are separated into two different compartments of the separation container. The numerical model of the sorter, shown in Fig.3 b, is an exact replication of the described sorting system.

3.2. Particle approximation

Three different bulk solids are investigated in this study, namely peppercorns, maize grains and coffee beans. They were selected due their easy accessibility, importance in the optical sorting industry and difference in size, shape and density. Peppercorns are employed for the base case of this study and are therefore also used in the conducted experiments, due to their irregular movement on the conveyor belt. This makes the sorting task especially difficult and allows a detailed analysis

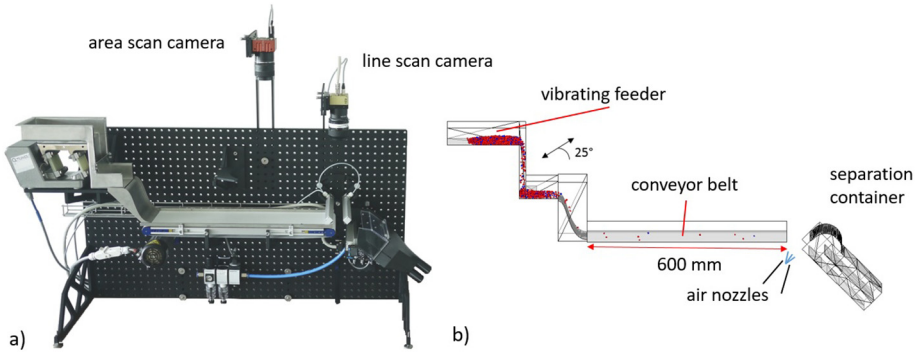

Fig.3. Experimental a)and numerical b)setup of the optical belt sorter.

of the advantages of utilizing an area scan camera in combination with particle tracking.

The first step in modelling these bulk solids within the DEM is to determine a size, volume and density distribution for each of the particle types. In order to approximate the particle shape, shadow projections of the different materials are created, and five particle shape types are generated for each of the bulk solids. This is done with a MATLAB script by filling the depicted particle outline with 8 to 10 spheres, depending on the complexity of the shape. The process can be seen in Fig.4, exemplary for peppercorns. To ensure a correct representation of the packing structure and local solid fraction distribution within a particle packing and therefore the overall approximation quality, a volume-based size distribution with five different particle sizes is considered.

In addition to the particle shape and size, important DEM parameters describing the particle–particle and particle–wall interactions have to be defined. These include the coefficients of normal restitution, Coulomb friction and rolling friction and are initially determined experimentally by assembling the results from a sufficient number of single particle events according to procedures described by Höhner etal. [57] and Sudbrock etal. [58]. For particle–wall contacts, the steel used for the vibrating feeder and slide of the sorter as well as the material of the conveyor belt were considered.

As the determination of precise and reliable interaction parameters based on individual particle impacts is almost impossible due to the high fluctuations of the results obtained from actual systems, the obtained values are merely used as a starting point for further optimization. As described in [41], further tests were conducted and compared with corresponding simulations. In order to analyze the parameters in a static scenario, a defined amount of each particle type is filled into a stationary cylinder, which was previously placed on a surface made of steel or conveyor belt material, depending on the investigate particle–wall pairing. In order to prevent any particles falling off the test rig, a second, wider ring is placed around the cylinder. When the material has settled, the cylinder is lifted upwards with a defined velocity and the particles form a pile on the respective surface material. The resulting angle of repose is averaged for both sides of the pile and compared between simulation and experiment, see Fig.5.

In a second step, a dynamic scenario is investigated, where one third of the volume of a rotary drum, outlined with steel or conveyor belt material, depending on the particle–wall pairing, is filled with one of the materials. The drum is then rotated with a constant velocity and the resulting angle of repose is again compared between experiment and simulation, see Fig.6.

After comparing the angles of repose between experiment and simulation for both the static and dynamic scenario, the initial DEM interaction parameters are automatically adjusted and another simulation for both cases is performed. The resulting angles are compared again and the process is repeated until the employed parameters result in matching angles of repose for both the static and dynamic scenario. The final particle parameters for all three particle types are presented in Table 1. It was found that defining the rolling friction coefficient equal for all contact forms of the respective bulk solid resulted in a good fit between experiment and simulation.

The DEM simulations are performed with a time step of $1 \cdot 10^{-5}$ s while a maximum particle overlap of 0.5% is ensured. The spring stiffness k^n and k^t as well as the damping coefficient γ^n are calculated from the chosen time step and the coefficient of restitution.

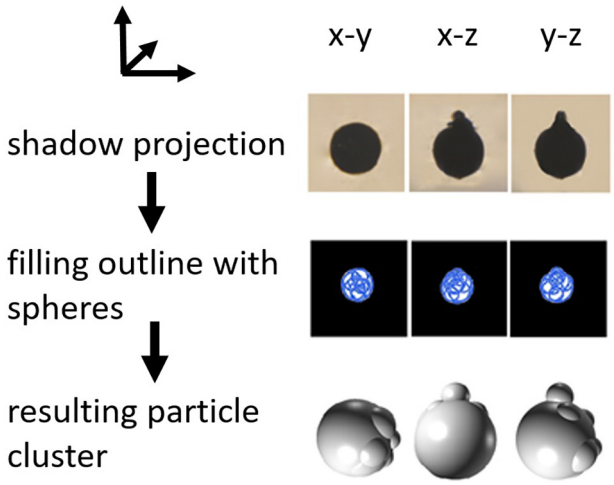

Fig.4. Peppercorn approximation for the DEM.

3.3. Nozzle bar

To simulate the fluid flow within the air nozzle and in the flow field established at the nozzle outlet, a hexagonal mesh of the air nozzle interior and the adjacent airspace is created. A CAD model of the nozzle bar employed in the modular optical belt sorter, see Fig.7 a, is used to generate the basic nozzle geometry, as shown in Fig.7 b. Only one of the sixteen nozzles is considered. The nozzle has one inlet and splits up into four nozzle outlets to cover the entire width of the conveyor belt.

A pressure inlet is defined at the nozzle inlets and a pressure outlet at the far-field boundary of the flow domain, see Fig.7 c. A gauge pressure of 1.2 bar is applied at the pressure inlet and the adjacent room is filled with quiescent air. To maintain feasible calculation times and to simplify the coupling between the DEM–CFD, a stationary flow field is assumed, while the fluid considered incompressible. Investigations showed that the steady state flow profiles obtained match well with results from transient calculations. Performing the simulation with acompressible fluid also produced very similar results. A standard k-εturbulence model is employed. The air has a density of $\rho_f = 1.225$ kg/m^2, viscosity of $\mu_f = 1.7894 \cdot 10^{-5}$ kg/(m·s) and a temperature of T_f= 293.15 K.

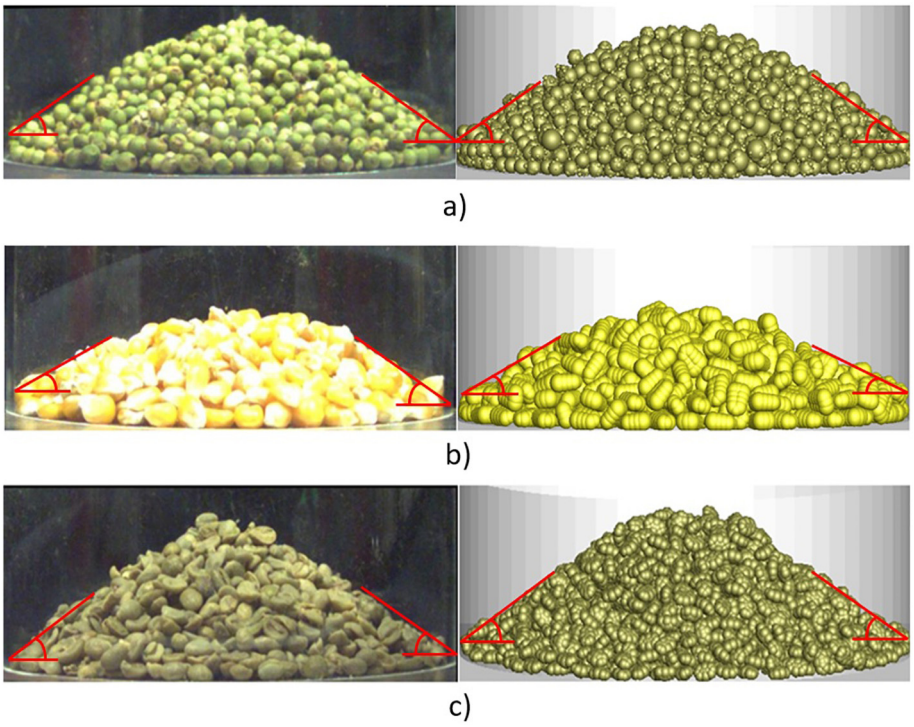

Fig.5. Angle of repose compared between experiment (left) and simulation (right) for a)peppercorns, b)maize grains and c)coffee beans, static scenario.

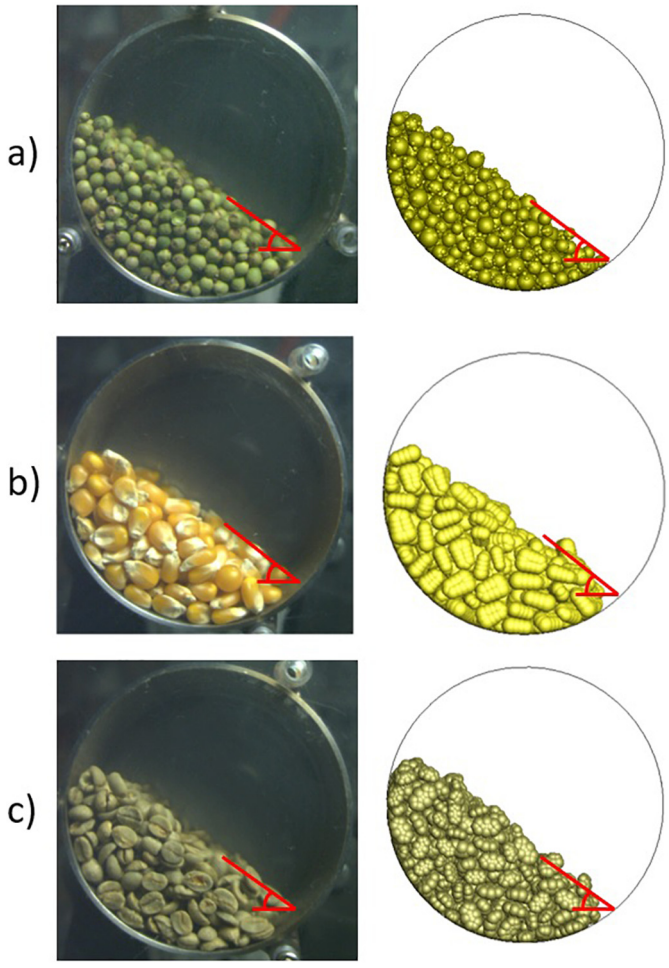

Fig.6. Angle of repose compared between experiment (left) and simulation (right) for a) peppercorns, b)maize grains and c)coffee beans, dynamic scenario.

Once the CFD calculation has converged, the resulting fluid data is prepared for utilization within the DEM. As the resolution of the mesh is very fine with 1.86 million cells and would result in very long simulation durations when used in the DEM, the fluid properties are averaged to larger cells. In addition, the flow field is trimmed to fit the air jet contours, which also reduces the number of fluid cells and therefore speeds up the calculation. The new fluid cells have a dimension of $2 \times 2 \times 2$ mm^3 and cover a total volume of $20 \times 50 \times 150$ mm^3. To model the entire nozzle bar, the fluid cell zone determined for a single nozzle is duplicated sixteen times to form one large mesh, now consisting of 159,375 cells. When a particle enters the zone where the fluid cells are coupled with the DEM, the fluid properties of every fluid cell that lies within the particle boundary are averaged and used to compute the particle–fluid force as described in Section2.1.

In order to validate the CFD simulation conducted, the calculated fluid velocity field is compared with experimental measurements of the flow field in front of an individual nozzle of the nozzle bar. The measurements are performed with a pitot tube, which is mounted on a table that can be automatically moved in all three main coordinate directions in small increments. A slice on the $x - y$ plane, located 20 mm in front of an individual nozzle is considered, see Fig.8. This is the distance at which the particle–fluid interaction at the separation stage of the sorter takes place. The results of the experimental measurements are shown in Fig.8 a and those of the corresponding simulation in Fig.8 b. The obtained data shows that there is good agreement between experiment and simulation with respect to both the area of influence of the air jets and the velocity magnitude.

3.4. Prediction models

In this study, three different prediction models, defined as the method to predict the particles' future motion after leaving the detection phase of the sorter, are employed and compared. In all three cases, the final prediction is made when the particles reach the end of the conveyor belt. This is defined as the detection stage for the line scan camera and ideal constant velocity (CV) prediction model. The separation stage of the sorter is located 0.075 m behind the belt end.

Table1
Particle properties of peppercorns, maize grains and coffee beans required for the DEM simulations.

Shape	Peppercorns	Maize grains	Coffee beans
			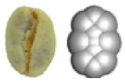
Average mass [g]	0.0272	0.2624	0.0915
Average density [kg/m^2]	551.47	1212.12	1041.67
Restitution coefficient PP [−]	0.627	0.705	0.63
Restitution coefficient PW sorter [−]	0.721	0.349	0.492
Restitution coefficient PW belt[−]	0.701	0.349	0.492
Friction coefficient PP [−]	0.4	0.2	0.3
Friction coefficient PW sorter [−]	0.326	0.352	0.337
Friction coefficient PW belt [−]	0.336	0.377	0.357
Rolling friction coefficient PP [m]	0.00008	0.00004	0.00004
Rolling friction coefficient PW sorter [m]	0.00008	0.00004	0.00004
Rolling friction coefficient PW belt [m]	0.00008	0.00004	0.00004

The most common and basic principle, which is also used in most state-of-the-art industrial sorters, is referred to as the line scan camera model, see Fig.9 a. Here it is assumed that the particles only move in belt direction and have no cross movements. The predicted particle velocity at the end of the detection stage v_{pr} is assumed to be equal for all particles and is determined by averaging the velocity of every particle at the end of the detection stage $\overline{v}_{pr}$, in a preliminary simulation. These boundary conditions are directly considered within the DEM and no coupling with the tracking algorithm is performed for these simulations.

The second procedure is referred to as the tracking model, see Fig.9 b. This method is based on the utilization of an area scan camera for particle detection, where particle positions and velocities are assessed over multiple points in time (v_{t1}, $v_{t2,}$...v_{tn}), and the tracking algorithm, based on a CV model, for the prediction of the particles' future motion. In the simulation, the DEM–CFD is coupled with the MATLAB tracking script as described in section 2.3.

In the third method employed, the particle velocity and direction of movement at the end of the detection phase is directly taken from the DEM calculations, as shown in Fig.9 c. In the course of this study this

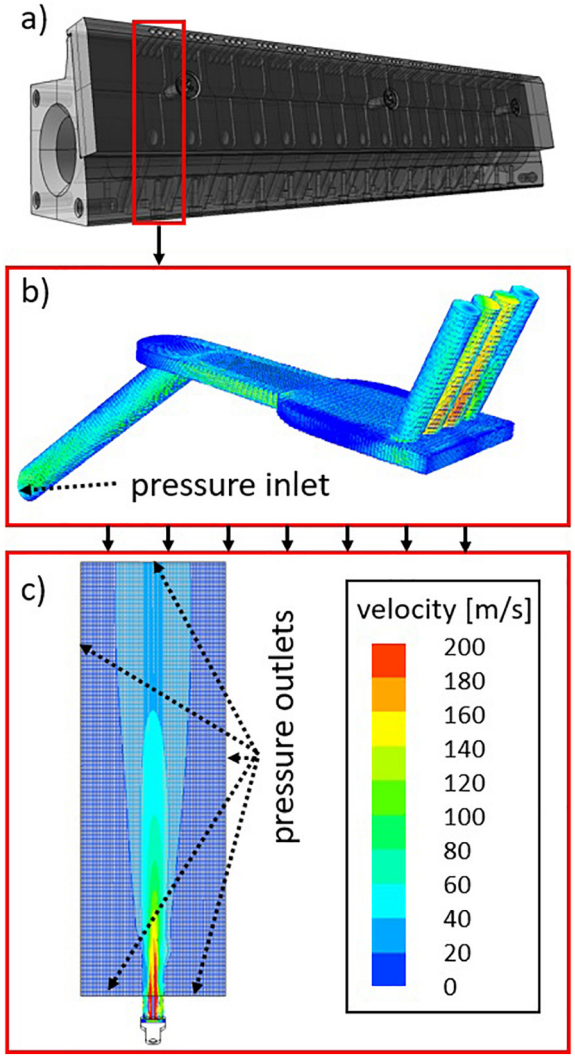

Fig.7. Air nozzle mesh b)derived from a CAD model of the sorting system nozzle bar a)and resulting fluid field c).

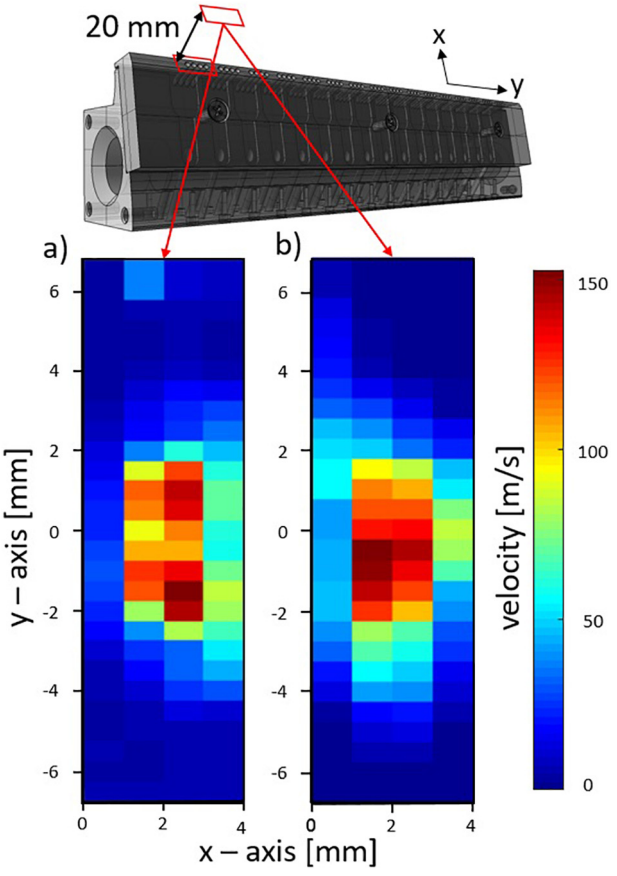

Fig.8. Comparison of fluid velocity fields for experiment a)and simulation b)20 mm in front of an individual nozzle.

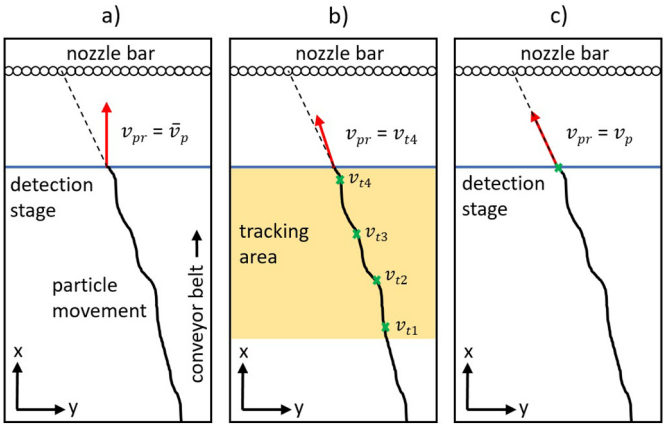

Fig.9. Visualization of the employed prediction models, a)line scan camera, b)tracking, c) ideal CV prediction.

method is referred to as the ideal constant velocity prediction model (ideal CV). By default, this is the most accurate information on the particle movement and the model is used to benchmark the two other prediction procedures.

3.5. Operational procedure

In order to compare the resulting sorting quality for the three prediction models, a base case is defined and five operational parameters are altered one at a time in different simulation series. On the DEM–CFD side, these parameters include the conveyor belt length, nozzle activation duration and the particle type. On the tracking side, the dimension of the area in which the particle positions are transferred to the tracking algorithm and the frequency of these exchanges are investigated. An overview of the parameters varied is presented in Table 2. The highlighted values represent the base case of the study.

At the start of each simulation, 50 g of peppercorns are placed in a container positioned on the vibrating feeder, which is operated at an amplitude of 0.278 mm. When maize grains and coffee beans are employed, 200 g are used due to the higher density and size of the particles compared to the peppercorns. The assembled bulk solids always consist of 80% blue particles and 20% red particles, the latter set to be separated from the material stream. This ratio was chosen as a compromise between typical real-world applications and a sufficiently difficult sorting task. The initial particle packing within the container is generated randomly at the beginning of each simulation, resulting in an arbitrary mixture of red and blue particles. Before the container is lifted upwards, thereby releasing the particles onto the vibrating feeder, the particles settle under gravity and form a loose packing. After the bulk solids have moved through the sorter, the resulting separation quality is assessed and compared. All simulations are conducted three times, each time with a different, randomly generated particle packing.

4. Results and discussion

4.1. Initial validation

In order to ensure that the particle approximation and the particle parameters determined are sufficiently accurate to model the particle behavior within the optical sorter, the mass flow of peppercorns is measured both experimentally and numerically. Peppercorns were chosen exemplary, as they are the bulk solids used in the base case of the study. As the mass flow rate is highly dependent on the vibrating feeder amplitude, a high-speed camera is used to analyze the amplitude, angle and frequency of the induced vibration in detail. Results show that the frequency and vibration-angle are constant with values of 50 Hz and 25° respectively. The amplitude can be regulated with a transformer and three amplitudes of $a_1 = 0.402$ mm, $a_2 = 0.278$ and $a_3 = 0.236$ were measured and then used for the comparison.

Table2
Investigated operational parameters with the base case of the study highlighted in green.

Conveyor belt length [m]	Nozzle activation duration [s]	Particle type [-]	Tracking window length [m]	Detection frequency [Hz]
0.45	0.0025	Maize grains	0.05	100
0.30	0.005	Peppercorns	0.1	200
0.6	0.01	Coffee beans	0.15	300

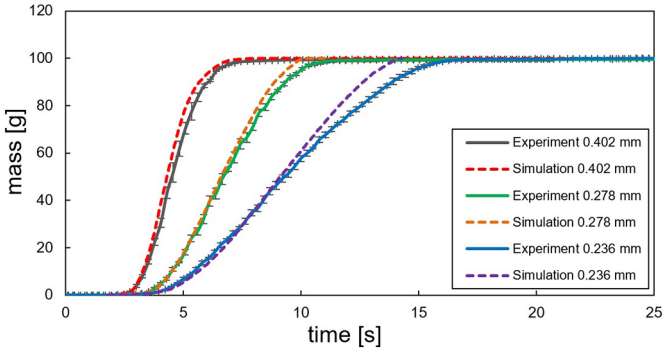

Fig.10. Exiting particle mass of peppercorns for different operating amplitudes compared between experiment and simulation.

To measure the exiting particle mass flow in the experimental setup, a scale with a collecting container is positioned at the end of the conveyor belt. Both the air nozzles as well as the separation container are removed during the procedure. At the start of the experiment, the same initialization procedure used for the separation investigation described in Section3.5 is employed. 100 g of peppercorns are used and the measurement is repeated three times for each investigated amplitude setting. The results are shown in Fig.10.

The figure shows that there is good agreement between the DEM simulations and the conducted experiments. Slight offsets can be seen at the end of the process, especially for small amplitudes. Here, the peppercorns in the simulation exit the system at a faster pace. Further investigation showed that this is likely due to small irregularities and dents on the surface of the vibrating feeder of the experimental setup. These imperfections cause particle movement to slow down, especially when the peppercorns no longer move in bulk.

In a next step, the actual sorting result is compared between an experimental and numerical setup. The experiment is carried out first, according to the procedure described in Section3.5. In the experimental investigation, a line scan camera is located at the end of the belt. The color of passing particles is detected and depending on the *y*-location of the peppercorn, a specific nozzle is activated. The delay between particle detection and nozzle activation is calculated by assuming that the particle is moving with belt velocity. Particle movement orthogonal to the belt is neglected. In the simulation, the line scan camera model is used. It is important to keep in mind that the goal of the conducted experiment is not to achieve a perfect separation quality, but to ensure that defined system parameters are used that can be transferred to thenumerical setup. The system was deliberately run under difficult operating conditions and with a high particle feed rate in order to properly test the numerical accuracy. The experiment is conducted three times.

After the sorting process is complete, the peppercorns are extracted from the separation container and the separation quality is assessed by weighing the different particle fractions. This is of course not necessary for the simulation where the sorting result is directly written to a text file.

The findings of the conducted experimental and numerical sorting process and its comparison are presented in Fig.11. The error bars represent the standard deviation of the three conducted experiments. The results show that there is generally good agreement between the

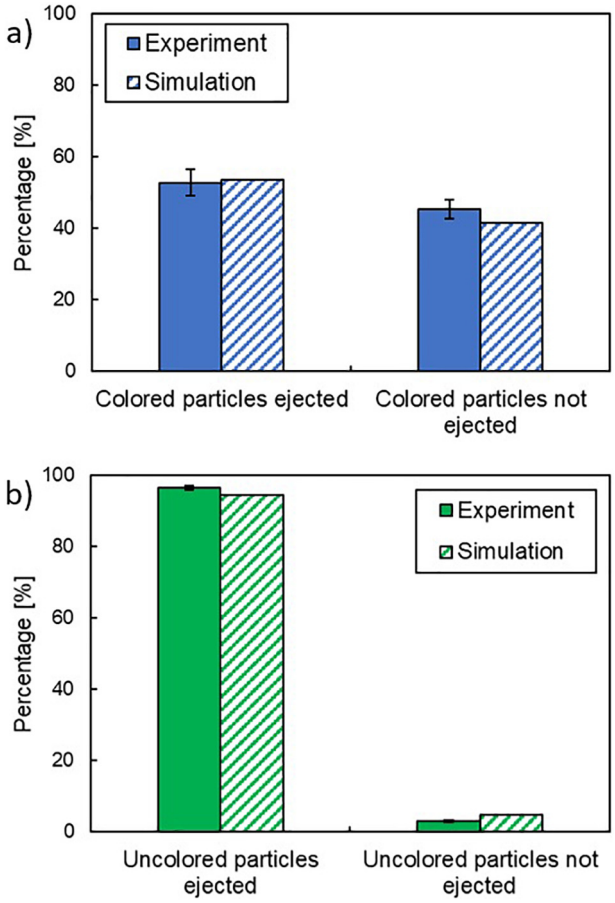

Fig.11. Comparison of particle separation results between experiment and simulation for a)ejected/not ejected colored particles and b)ejected/not ejected uncolored particles.

experiment and simulation. Fig.11 a shows the percentage of the colored peppercorns ejected and not ejected from the material stream. The amount of particles ejected is only slightly higher for the simulation, which is most likely due to the fact that a small amount of particles is not correctly identified by the line scan camera. This is of course not the case in the simulation. The separation results of the uncolored particles can be seen in Fig.11 b. Only a small amount of by-catch is produced and the simulation differs from the results obtained from the experiment only by a very small margin.

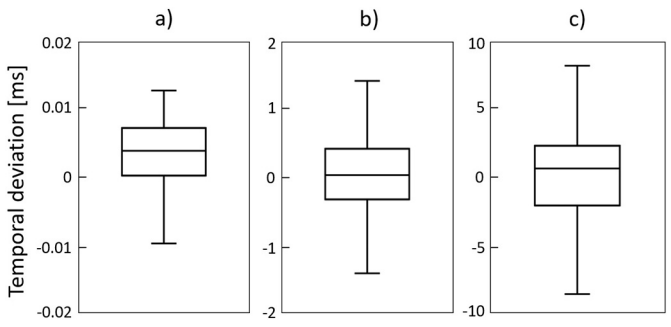

Fig.12. Temporal deviation from the actual particle position at the separation stage for the a)ideal CV prediction, b)tracking and c)line scan camera model. The line in the middle indicates the median, the box represents 50% of the data and the whiskers the upper and lower 25% of the data.

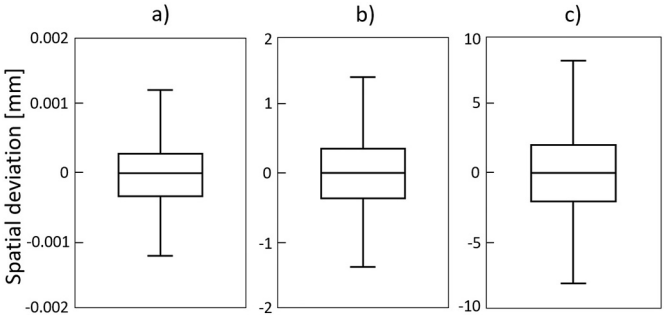

Fig.13. Spatial deviation from the actual particle position at the separation stage for the a) ideal CV prediction, b)tracking and c)line scan camera model. The line in the middle indicates the median, the box represents 50% of the data and the whiskers the upper and lower 25% of the data.

4.2. Prediction accuracy of the models employed

The base case of the study is utilized as the basis for the accuracy analysis and in a first step, a simulation without particle separation is conducted. The exact time and place of when and where each particle reaches the separation unit is stored and used as a ground truth for the comparison of the prediction models. The predictions made for every particle are then compared with the established ground truth and average deviations are determined for each of the three methods. The results are presented as box plots and outliers with a deviation of more than 1.5 times the interquartile range are omitted.

The temporal deviation of the employed models is presented in Fig.12. The results show that the prediction error of the time in which the particles reach the separation unit is smallest for the ideal CV prediction, Fig.12 a, utilizing the velocity and movement direction at the end of conveyor belt directly from the DEM, with deviations ranging from −0.01 ms to 0.013 ms. This is followed by the tracking model, Fig.12 b, already with significantly larger errors in the range of −1.4 ms to 1.4 ms. The line scan camera method, Fig.12 c, shows the largest deviation, namely −8 ms to 8 ms. The fact that the median of the data sets is slightly higher than zero, is attributed to the fact that the particles start to slow down after leaving the conveyor belt. This is not considered by the prediction models, but constitutes a first optimization feature.

The spatial deviation of the investigated prediction models is shown in Fig.13. The trend observed in the evaluation of the temporal deviation can also be found here, namely that the ideal CV prediction, Fig.13 a, shows the smallest error, followed by the tracking model, Fig.13 b, and the line scan camera model Fig.13 c.

The comparison of the prediction accuracy of the models employed already shows that the tracking procedure delivers promising results, and is able to determine the future particle position much more

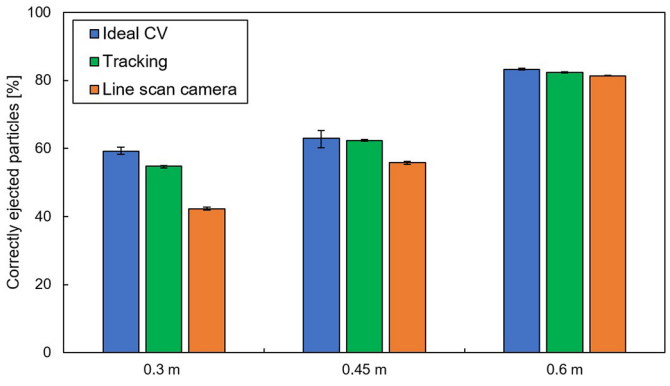

Fig.14. Percentage of correctly ejected particles for different conveyor belt length.

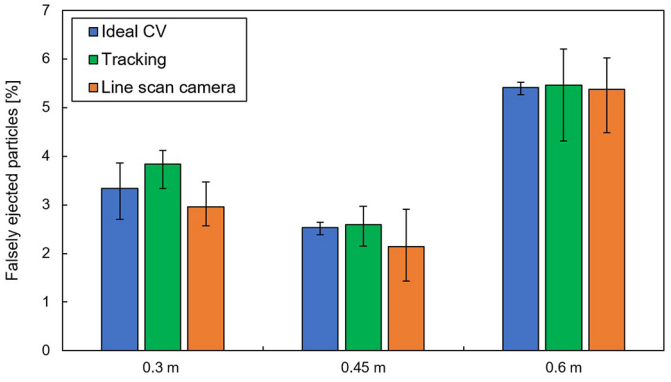

Fig.15. Percentage of falsely ejected particles for different conveyor belt lengths.

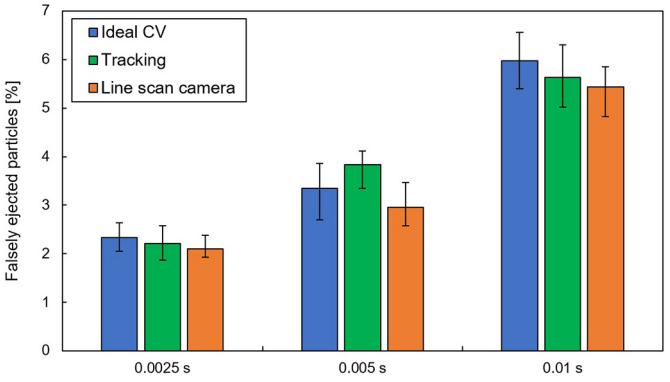

Fig.17. Percentage of falsely ejected particles for different nozzle activation durations.

precisely than the conventional assumptions used when operating a line scan camera system. However, these findings are still of a theoretical nature, and the influence on the actual sorting quality of the system remains to be investigated. This is done in the following sections.

4.3. Influence of conveyor belt length

Three different belt lengths are considered, namely 0.3 m, 0.45 m and 0.6 m. The percentages of correctly ejected particles are presented in Fig.14. With increasing belt length, the number of correctly ejected particles rises for all three prediction models. A longer belt reduces the cross movement of the material and also leads to a more consistent particle velocity distribution. This greatly reduces the difficulty of the separation task. The findings show that employing the tracking model results in a higher percentage of correctly ejected particles compared with the line scan camera model in all three investigated cases. This advantage is especially pronounced at the shorter belt lengths, where the particles have not fully obtained the belts velocity and direction of movement.

The percentage of falsely co-ejected particles, also referred to as by-catch, is shown in Fig.15. In contrast to the results of the correctly ejected particles, no distinct trend is visible and the error bars are comparably high. In order to assess the meaning of these results, it is important to consider that altering the belt length of the sorter directly affects other system parameters. As the particle velocity at the end of the belt is highly dependent on the length of the belt, the nozzle bar and the separation container have to be readjusted for each simulation. In addition, the velocity of individual particles at the end of the belt deviates much more from the mean particle velocity at shorter belt lengths. This entails that the separation container has to be placed further away from the mean particle trajectory, which makes it harder to eject the desired material but also causes a reduction of by-catch. A detailed investigation of the connection between correctly and falsely ejected particles is, however, not part of this study.

4.4. Influence of nozzle activation duration

Nozzle activation durations of 0.0025 s, 0.005 s and 0.01 s are considered. The percentage of the correctly ejected particles is presented in Fig.16. As expected, the figure shows that the amount of correctly ejected particles increases with longer activation durations for all three investigated prediction models. Employing the tracking model leads to superior separation results compared to the line scan camera model in all three cases. Here, it is interesting to note that the difference between the two models remains almost equal with about 17%, at all investigated activation durations. This shows that the overall advantage of utilizing an area scan camera combined with particle tracking is especially useful when employing low nozzle activation durations.

The percentages of falsely ejected particles for the different nozzle activation durations are presented in Fig.17. Increasing the activation duration naturally also leads to an increase in falsely co-ejected particles. This trend is consistent for all prediction models. Again, no correlation can be found between the observed by-catch and employed prediction model.

4.5. Influence of particle type

Peppercorns, maize grains and coffee beans are employed as different particle types. The percentage of correctly ejected particles is presented in Fig.18. The results show that the share of correctly ejected material is significantly higher for maize grains and coffee beans compared with the peppercorns. This can be explained by two main factors, namely the particle movement on the conveyor belt and the particle size. While the peppercorns have a nearly spherical shape, which

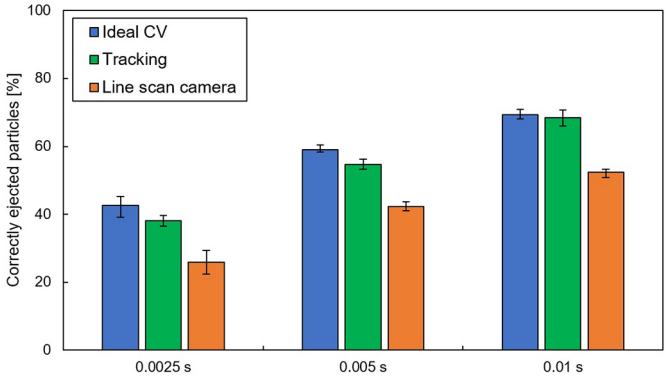

Fig.16. Percentage of correctly ejected particles for different nozzle activation durations.

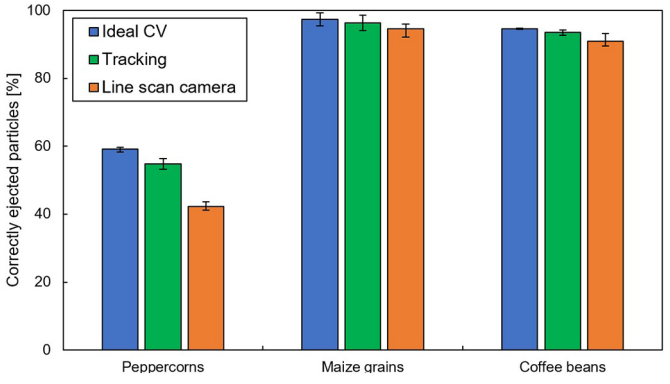

Fig.18. Percentage of correctly ejected particles for different particle type.

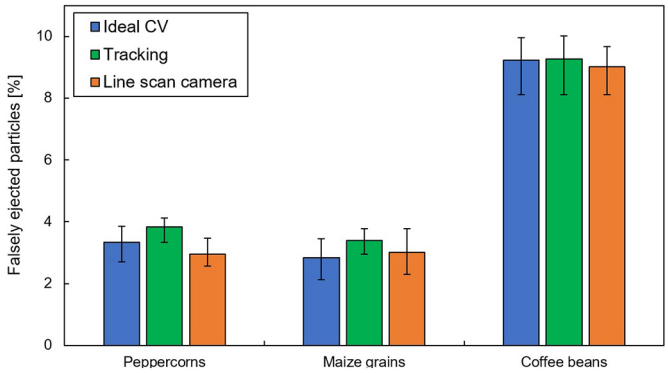

Fig.19. Percentage of falsely ejected particles for different particle type.

induces a profound proper motion on the conveyor belt, the maize grains and coffee beans have an almost flat surface area, causing them to adapt to the belt velocity and direction of movement much faster. In addition, the increased particle size offers a larger surface area for the air jet to hit the material. However, even at these high ejection rates, the tracking model still outperforms the line scan camera by a margin of 2–4% for both the maize grains and coffee beans.

The percentage of falsely ejected particles is presented in Fig.19. The results show that the by-catch of the coffee beans is considerable higher compared with the other two particles types. Considering that the percentage of correctly ejected particles is almost equal for maize grains and coffee beans, this difference seems unusual. However, to account for the 200 g of employed material, about 763 maize grains and 2186 coffee beans are required. This leads to a significantly higher belt load and closer particle proximity in the coffee bean simulations, which is directly related to the increase of by-catch.

4.6. Influence of tracking parameters

The effect of altering different tracking parameters, namely the detection frequency and length of the detection window (see section 2.3), on the separation quality is investigated in the final simulation series.

Three detection frequencies, 100 Hz, 200 Hz and 300 Hz are considered. The percentage of the correctly ejected particles is shown in Fig.20 a. The results obtained indicate that a higher sampling frequency generally improves the ejection accuracy. However, the additional benefit from utilizing a 300 Hz camera over the 200 Hz model available for the table sort setup is not very significant. This shows that there is not necessarily the need for an expensive high speed camera and that the amount of data required for a precise tracking prediction is manageable. The percentage of falsely ejected particles, see Fig.20 b, supports these conclusions.

The results of altering the length of the detection window employed, namely 5 cm, 10 cm and 15 cm, are presented in Fig.21. The percentage of correctly ejected particles, see Fig.21 a, and falsely ejected particles, see Fig.21 b, shows that there is only a slight improvement when employing a larger detection area. This also underlines the assumption that already a small amount of particle data is sufficient for a significant prediction improvement, as shown in the previous sections of this study.

5. Conclusions

A numerical model of an automated optical belt sorter based on a coupled DEM–CFD approach was described and the impact of employing different operating parameters and prediction models on the sorting quality was assessed. Three bulk solids, namely peppercorns, maize grains and coffee beans were modelled with a multi-sphere particle approximation and the particle interaction parameters required were determined in comprehensive experimental and numerical investigations. The utilized nozzle bar was described with a FVM approach and the resulting fluid velocity field was compared with measurements of corresponding experiments. To benchmark the novel prediction method, designated as predictive tracking, the DEM–CFD was coupled with a MATLAB script running the tracking algorithm. The following conclusions can be drawn from this study:

- The methods employed to model complex-shaped bulk solids and to define the required DEM parameters shows good results when comparing the particle mass flow through the sorter between experiment and simulation.
- The approximation of the nozzle bar with a FVM approach seems suitable to model the separation stage of the optical sorter and shows good agreement with corresponding experiments. The one-way coupling of the DEM with CFD constitutes an important step in modelling the entire optical belt sorter.
- A comparison of separation results between the numerical and experimental sorting system reveals promising results and underlines that the numerical setup described and modelled in this study is suitable to investigate sorter performance under different operational conditions.
- Coupling the DEM–CFD with the devised tracking prediction model outperforms the state-of-the-art line scan camera method in all investigated parameter variations. The additional benefits of the new prediction procedure are especially profound when the sorting task is difficult. This is the case when a short belt length, a short nozzle activation duration and bulk solids with distinct proper motion on the conveyor belt, in this study the peppercorns, are employed.

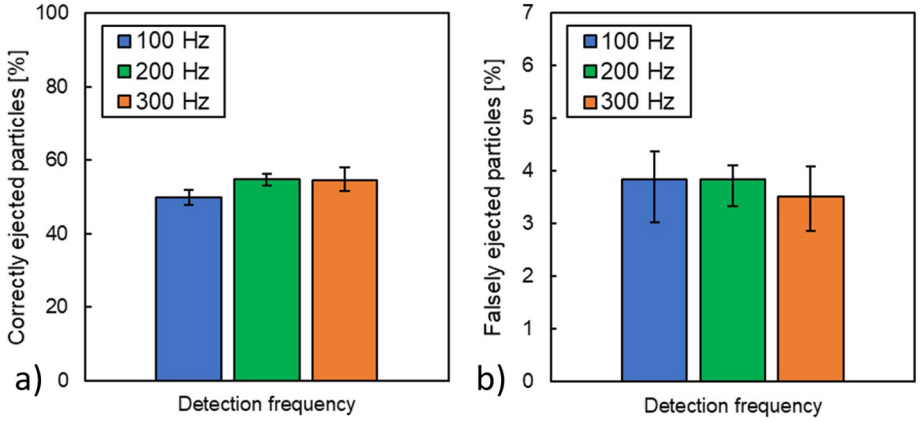

Fig.20. Correctly a)and falsely b)ejected particles for different detection frequencies.

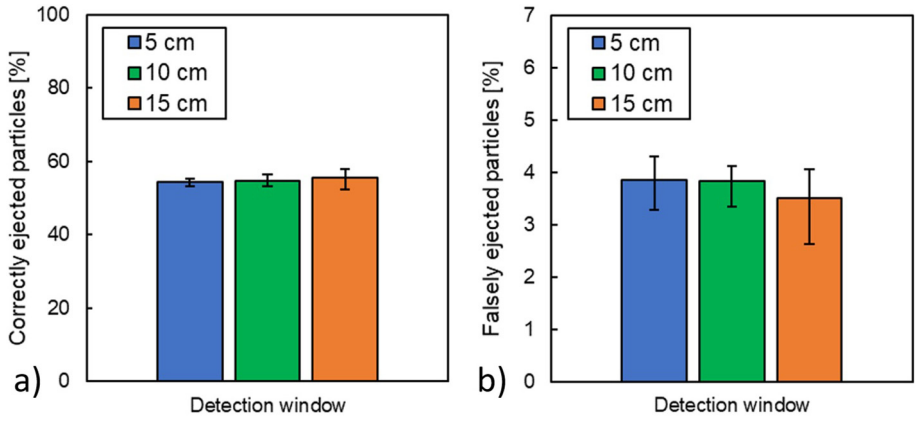

Fig.21. Correctly a)and falsely b)ejected particles for different detection windows.

- Correct evaluation of the percentage of falsely co-ejected particles and their connection to the prediction models used turned out to be rather difficult, as altering one system parameter often indirectly influences other sorter parameters. It can generally be concluded that in order to understand the complex interaction between falsely ejected particles and various system parameters, an additional, detailed study needs to be conducted.

In summary it can be said that the newly introduced method of accurately predicting the future particle position by the use of an area scan camera coupled with particle tracking, seems to be a very promising development in the field of optical sorting. The simulations conducted in this study emphasize the advantages of the technology in comparison to state-of-the-art line scan camera systems. However, it is important to note that the benefit of employing this technology will most likely be limited to specific and difficult sorting scenarios.

In a next step, the described prediction approach will be tested on the presented table sort system and similar investigations to this study will be conducted. If successful, the method will be applied to full size optical sorting systems.

Acknowledgements

The IGF project 18798 N of the research association Forschungs-GesellschaftVerfahrens-Technik e.V. (GVT) was supported via the AiF in a program to promote the Industrial Community Research and Development (IGF) by the Federal Ministry for Economic Affairs and Energy on the basis of a resolution of the German Bundestag.

References

[1] M. Graves, B. Batchelor (Eds.), Machine vision for the inspection of natural products, Springer-Verlag, London, 2003https://doi.org/10.1007/b97526.
[2] D.M. Dehler, Optische Sortierung von Quarzkieseln zur Senkung des Eisengehaltes, Aufbereitungstechnik 47 (2006) 6–8.
[3] S.R. Delwiche, T.C. Pearson, D.L. Brabec, High-speed optical sorting of soft wheat for reduction of deoxynivalenol, Plant Dis. 89 (2005) 1214–1219, https://doi.org/10.1094/PD-89-1214.
[4] K. Bilir, H. Akdas, Evaluation of magnesite wastes using optical sorting machine, Proc. XIII. Int. Miner. Process. Symp 2012, pp. 1017–1023.
[5] F. Brandt, R. Haus, New concepts for lithium minerals processing, Miner. Eng. 23 (2010) 659–661, https://doi.org/10.1016/j.mineng.2010.03.021.
[6] M. Dehler, Optical sorting of ceramic raw material, Tile Brick Int. 19 (2003) 248–251.
[7] M. Dehler, Wedel, Optische Sortierung von mineralischen Rohstoffen, Schüttgut 10 (2004) 212–216.
[8] F.E. Dowell, T.N. Boratynski, R.E. Ykema, A.K. Dowdy, R.T. Staten, Use of optical sorting to detect wheat kernels infected with tilletia indica, Plant Dis. 86 (2011) 500–502.
[9] R.P. Haff, T.C. Pearson, E. Maghirang, A multispectral sorting device for isolating single wheat kernels with high protein content, J. Food Meas. Charact. 7 (2013) 149–157, https://doi.org/10.1007/s11694-013-9150-7.
[10] L.A. Paluchowski, E. Misimi, L. Grimsmo, L.L. Randeberg, Towards automated sorting of Atlantic cod (Gadus morhua) roe, milt, and liver - Spectral characterization and classification using visible and near-infrared hyperspectral imaging, Food Control 62 (2016) 337–345, https://doi.org/10.1016/j.foodcont.2015.11.004.
[11] S.P. Gundupalli, S. Hait, A. Thakur, A review on automated sorting of source-separated municipal solid waste for recycling, Waste Manag. 60 (2017) 56–74, https://doi.org/10.1016/j.wasman.2016.09.015.
[12] M. Bigum, L. Brogaard, T.H. Christensen, Metal recovery from high-grade WEEE: a life cycle assessment, J. Hazard. Mater. 207–208 (2012) 8–14, https://doi.org/10.1016/j.jhazmat.2011.10.001.
[13] S. Brunner, P. Fomin, C. Kargel, Automated sorting of polymer flakes: fluorescence labeling and development of a measurement system prototype, Waste Manag. 38 (2015) 49–60, https://doi.org/10.1016/j.wasman.2014.12.006.
[14] N. Dias, I. Garrinhas, A. Maximo, N. Belo, P. Roque, M.T. Carvalho, Recovery of glass from the inert fraction refused by MBT plants in a pilot plant, Waste Manag. 46 (2015) 201–211, https://doi.org/10.1016/j.wasman.2015.07.052.
[15] E. Scavino, D.A. Wahab, A. Hussain, H. Basri, M.M. Mustafa, Application of automated image analysis to the identification and extraction of recyclable plastic bottles, J. Zhejiang Univ. A 10 (2009) 794–799, https://doi.org/10.1631/jzus.A0820788.
[16] J.D. Salter, N.P.G. Wyatt, Sorting in the minerals industry: past, present and future, Miner. Eng. 4 (1991) 779–796, https://doi.org/10.1016/0892-6875(91)90065-4.
[17] G. Ligus, Municipal waste management model with the use of optical sorting elements, Chem. Aust. 66 (2012) 1229–1234.
[18] J.R. Mathiassen, E. Misimi, M. Bondø, E. Veliyulin, S.O. Østvik, Trends in application of imaging technologies to inspection of fish and fish products, Trends Food Sci. Technol. 22 (2011) 257–275, https://doi.org/10.1016/j.tifs.2011.03.006.
[19] A. Müller, Bauschutt ohne Gips, Steinbruch Und Sandgrube 11 (2012) 40–45.
[20] J. Nakatani, K. Konno, Y. Moriguchi, Variability-based optimal design for robust plastic recycling systems, Resour. Conserv. Recycl. 116 (2017) 53–60, https://doi.org/10.1016/j.resconrec.2016.09.020.
[21] D.M. Scott, A two-colournear-infrared sensor for sorting recycled plastic waste, Meas. Sci. Technol. 6 (1995) 156–159, https://doi.org/10.1088/0957-0233/6/2/004.
[22] D.M. Scott, R.L. Waterland, Identification of plastic waste using spectroscopy and neural networks, Polym. Eng. Sci. 35 (1995)https://doi.org/10.1002/pen.760351208.
[23] M.A. Zulkifley, M.M. Mustafa, A. Hussain, A. Mustapha, S. Ramli, Robust identification of polyethylene terephthalate (PET) plastics through bayesian decision, PLoS ONE 9 (2014) 1–20, https://doi.org/10.1371/journal.pone.0114518.
[24] R.D. Pascoe, O.B. Udoudo, H.J. Glass, Efficiency of automated sorter performance based on particle proximity information, Miner. Eng. 23 (2010) 806–812, https://doi.org/10.1016/j.mineng.2010.05.021.
[25] R.D. Pascoe, R. Fitzpatrick, J.R. Garratt, Prediction of automated sorter performance utilising a Monte Carlo simulation of feed characteristics, Miner. Eng. 72 (2015) 101–107, https://doi.org/10.1016/j.mineng.2014.12.026.
[26] R.S. Fitzpatrick, H.J. Glass, R.D. Pascoe, CFD–DEM modelling of particle ejection by a sensor-based automated sorter, Miner. Eng. 79 (2015) 176–184, https://doi.org/10.1016/j.mineng.2015.06.009.
[27] H.P. Zhu, Z.Y. Zhou, R.Y. Yang, a.B. Yu, Discrete particle simulation of particulate systems: theoretical developments, Chem. Eng. Sci. 62 (2007) 3378–3396, https://doi.org/10.1016/j.ces.2006.12.089.
[28] P.W. Cleary, M.D. Sinnott, R.D. Morrison, Separation performance of double deck banana screens - part 1: flow and separation for different accelerations, Miner. Eng. 22 (2009) 1218–1229, https://doi.org/10.1016/j.mineng.2009.07.002.
[29] K.J. Dong, A.B. Yu, I. Brake, DEM simulation of particle flow on a multi-deck banana screen, Miner. Eng. 22 (2009) 910–920, https://doi.org/10.1016/j.mineng.2009.03.021.
[30] J. Xiao, X. Tong, Characteristics and efficiency of a new vibrating screen with a swing trace, Particuology 11 (2013) 601–606, https://doi.org/10.1016/j.partic.2012.07.014.
[31] Z. Li, X. Tong, A study of particles penetration in sieving process on a linear vibration screen, Int. J. Coal Sci. Technol. 2 (2015) 299–305, https://doi.org/10.1007/s40789-015-0089-7.
[32] K.W. Chu, B. Wang, D.L. Xu, Y.X. Chen, A.B. Yu, CFD-DEM simulation of the gas-solid flow in a cyclone separator, Chem. Eng. Sci. 66 (2011) 834–847, https://doi.org/10.1016/j.ces.2010.11.026.

[33] K.W. Chu, B. Wang, A.B. Yu, A. Vince, G.D. Barnett, P.J. Barnett, CFD-DEM study of the effect of particle density distribution on the multiphase flow and performance of dense medium cyclone, Miner. Eng. 22 (2009) 893–909, https://doi.org/10.1016/j.mineng.2009.04.008.
[34] K.W. Chu, B. Wang, A.B. Yu, A. Vince, CFD-DEM modelling of multiphase flow in dense medium cyclones, Powder Technol. 193 (2009) 235–247, https://doi.org/10.1016/j.powtec.2009.03.015.
[35] F. Pfaff, M. Baum, B. Noack, U.D. Hanebeck, R. Gruna, T. Langle, J. Beyerer, TrackSort: Predictive tracking for sorting uncooperative bulk materials, IEEE Int. Conf. Multisens. Fusion Integr. Intell. Syst. (2015) 7–12, https://doi.org/10.1109/MFI.2015.7295737 Octob (2015).
[36] F. Pfaff, C. Pieper, G. Maier, B. Noack, H. Kruggel-Emden, R. Gruna, U.D. Hanebeck, S. Wirtz, V. Scherer, T. Längle, Improving Optical Sorting of Bulk Materials Using Sophisticated Motion Models, 2015https://doi.org/10.1515/teme-2015-0108.
[37] F. Pfaff, C. Pieper, G. Maier, B. Noack, H. Kruggel-Emden, R. Gruna, U.D. Hanebeck, S. Wirtz, V. Scherer, T. Langle, J. Beyerer, Simulation-based evaluation of predictive tracking for sorting bulk materials, in: IEEE Int, Conf. Multisens. Fusion Integr. Intell. Syst. (2017)https://doi.org/10.1109/MFI.2016.7849539.
[38] G. Maier, F. Pfaff, C. Pieper, R. Gruna, B. Noack, H. Kruggel-Emden, T. Langle, U.D. Hanebeck, S. Wirtz, V. Scherer, J. Beyerer, Fast multitarget tracking via strategy switching for sensor-based sorting, in: IEEE Int, Conf. Multisens. Fusion Integr. Intell. Syst. (2017)https://doi.org/10.1109/MFI.2016.7849538.
[39] C. Pieper, G. Maier, F. Pfaff, H. Kruggel-Emden, S. Wirtz, R. Gruna, B. Noack, V. Scherer, T. Längle, J. Beyerer, U.D. Hanebeck, Numerical modeling of an automated optical belt sorter using the Discrete Element Method, Powder Technol. 301 (2016)https://doi.org/10.1016/j.powtec.2016.07.018.
[40] H. Kruggel-Emden, S. Rickelt, S. Wirtz, V. Scherer, A study on the validity of the multi-sphere Discrete Element Method, Powder Technol. 188 (2008) 153–165, https://doi.org/10.1016/j.powtec.2008.04.037.
[41] F. Elskamp, H. Kruggel-Emden, M. Hennig, U. Teipel, A strategy to determine DEM parameters for spherical and non-spherical particles, Granul. Matter 19 (2017) https://doi.org/10.1007/s10035-017-0710-0.
[42] D. Höhner, S. Wirtz, H. Kruggel-Emden, V. Scherer, Comparison of the multi-sphere and polyhedral approach to simulate non-spherical particles within the discrete element method: Influence on temporal force evolution for multiple contacts, Powder Technol. 208 (2011) 643–656, https://doi.org/10.1016/j.powtec.2011.01.003.
[43] Y.C. Zhou, B.D. Wright, R.Y. Yang, B.H. Xu, A.B. Yu, Rolling friction in the dynamic simulation of sandpile formation, Phys. A Stat. Mech. Its Appl. 269 (1999) 536–553, https://doi.org/10.1016/S0378-4371(99)00183-1.
[44] K. Xue, K. Li, W. Chen, D. Chong, J. Yan, Numerical investigation on the performance of different primary nozzle structures in the supersonic ejector, Energy Procedia 105 (2017) 4997–5004, https://doi.org/10.1016/j.egypro.2017.03.1000.
[45] A.R. Gnana Sagaya Raj, J.M. Mallikarjuna, V. Ganesan, Energy efficient piston configuration for effective air motion - a CFD study, Appl. Energy 102 (2013) 347–354, https://doi.org/10.1016/j.apenergy.2012.07.022.
[46] H. Chu, R. Zhang, Y. Qi, Z. Kan, Simulation and experimental test of waterless washing nozzles for fresh apricot, Biosyst. Eng. 159 (2017) 97–108, https://doi.org/10.1016/j.biosystemseng.2017.05.001.
[47] R. Di Felice, The voidage function for fluid-particle interaction systems, Int. J. Multiphase Flow 20 (1994) 153–159, https://doi.org/10.1016/0301-9322(94)90011-6.
[48] A. Hölzer, M. Sommerfeld, New simple correlation formula for the drag coefficient of non-spherical particles, Powder Technol. 184 (2008) 361–365, https://doi.org/10.1016/j.powtec.2007.08.021.
[49] X.R. Li, V.P. Jilkov, Survey of maneuvering targettracking. Part I: dynamic models, IEEE Trans. Aerosp. Electron. Syst. 39 (2003) 1333–1364, https://doi.org/10.1109/TAES.2003.1261132.
[50] R.E. Kalman, A new approach to linear filtering and prediction problems, J. Basic Eng. 82 (1960) 35, https://doi.org/10.1115/1.3662552.
[51] S.M. Kay, Fundamentals of statistical signal processing: estimation theory, Prentice-Hall Signal Process. Ser. (1993) 595, https://doi.org/10.2307/1269750.
[52] R.P.S. Mahler, Statistical Multisource-Multitarget Information Fusion, 2007https://doi.org/10.1017/CBO9781107415324.004.
[53] S. Blackmann, Robert Popoli, Design and Analysis of Modern Tracking Systems, Artech House, 1999.
[54] R. Jonker, A. Volgenant, A shortest augmenting path algorithm for dense and sparse linear assignment problems, Computing 38 (1987) 325–340, https://doi.org/10.1007/BF02278710.
[55] D.P. Bertsekas, Auction Algorithm. Encycl. Optim. (2009) 128–132.
[56] G. Maier, F. Pfaff, M. Wagner, C. Pieper, R. Gruna, B. Noack, H. Kruggel-Emden, T. Längle, U.D. Hanebeck, S. Wirtz, V. Scherer, J. Beyerer, Real-time multitarget tracking for sensor-based sorting: a new implementation of the auction algorithm for graphics processing units, J. Real-Time Image Process. (2017)https://doi.org/10.1007/s11554-017-0735-y.
[57] D. Höhner, S. Wirtz, V. Scherer, Experimental and numerical investigation on the influence of particle shape and shape approximation on hopper discharge using the discrete element method, Powder Technol. 235 (2013) 614–627, https://doi.org/10.1016/j.powtec.2012.11.004.
[58] F. Sudbrock, E. Simsek, S. Rickelt, S. Wirtz, V. Scherer, Discrete element analysis of experiments on mixing and stoking of monodisperse spheres on a grate, Powder Technol. 208 (2011) 111–120, https://doi.org/10.1016/j.powtec.2010.12.008.